Supporting information

A green strategy for spent lithium-ion battery recycling via SO_2-driven cobalt reduction

Minyu He [a, b], Weizao Liu [a,*], Wen Cao [a], Xuewei Lv [a], Qingcai Liu [a], Charles Q. Jia [b,*]

[a] College of Materials Science and Engineering, Chongqing University, Chongqing 400044, China

[b] Department of Chemical Engineering and Applied Chemistry, University of Toronto, Toronto M5S 3E5, Canada

*Corresponding author: liuwz@cqu.edu.cn (W. Liu); cq.jia@utoronto.ca (Charles. Jia).

Supporting Information Content

23 pages (including the cover page)

18 Figures

6 Tables

5 Text

Figure S1. X-ray diffraction patterns of the cathode powder.

Figure S2. The corresponding enthalpy change (ΔH) of Reaction 1-4.

Figure S3. The "α-T" curves at different heating rates from room temperature to 200°C.

Figure S4. The "α-T" curves at different heating rates from 200°C to 500°C.

Figure S5. The linear fitting plots at different reaction stage through (a) FWO, (b) KAS, and (c) Starink methods.

Figure S6. The linear fitting plot of ln(k(T)-1/T and calculated activation energy in first stage.

Figure S7. The linear fitting plot of ln(k(T))-1/T and calculated activation energy in second

Text S2. Regeneration of LCO

Text S3. Economic and environmental analysis.

Text S4. Analysis method.

Text S5. Equilibrium calculations.

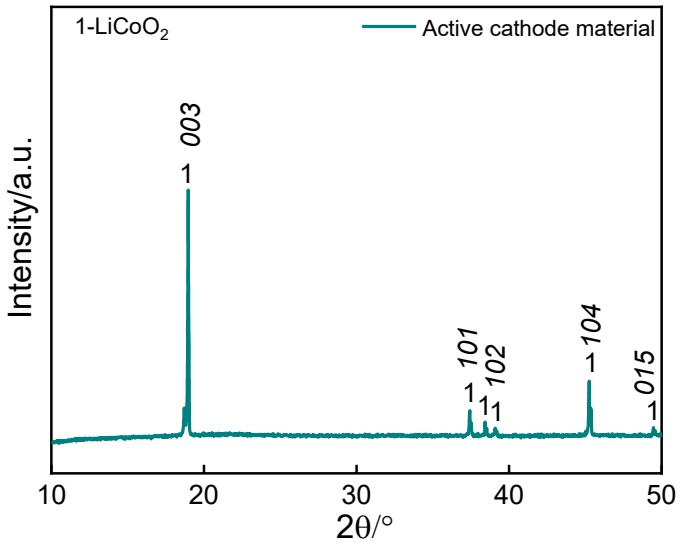

Figure S1. XRD pattern of the active cathode powder.

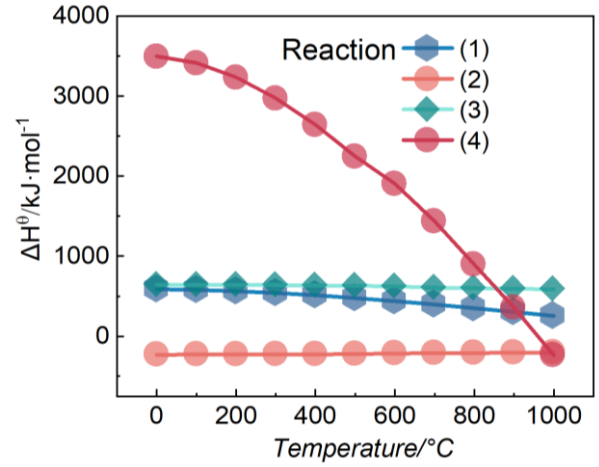

Figure S2. The corresponding enthalpy change (ΔH) of Reaction 1-4.

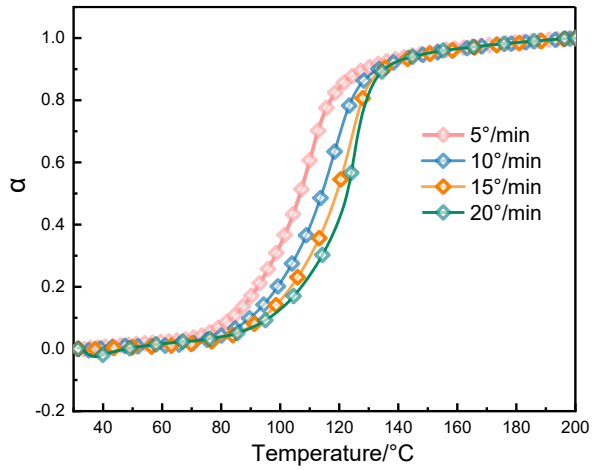

Figure S3. The “α-T” curves at different heating rates from room temperature to 200°C.

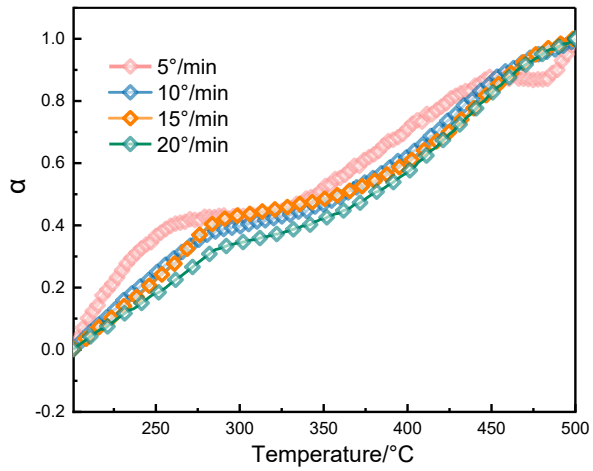

Figure S4. The “α-T” curves at different heating rates from 200°C to 500°C.

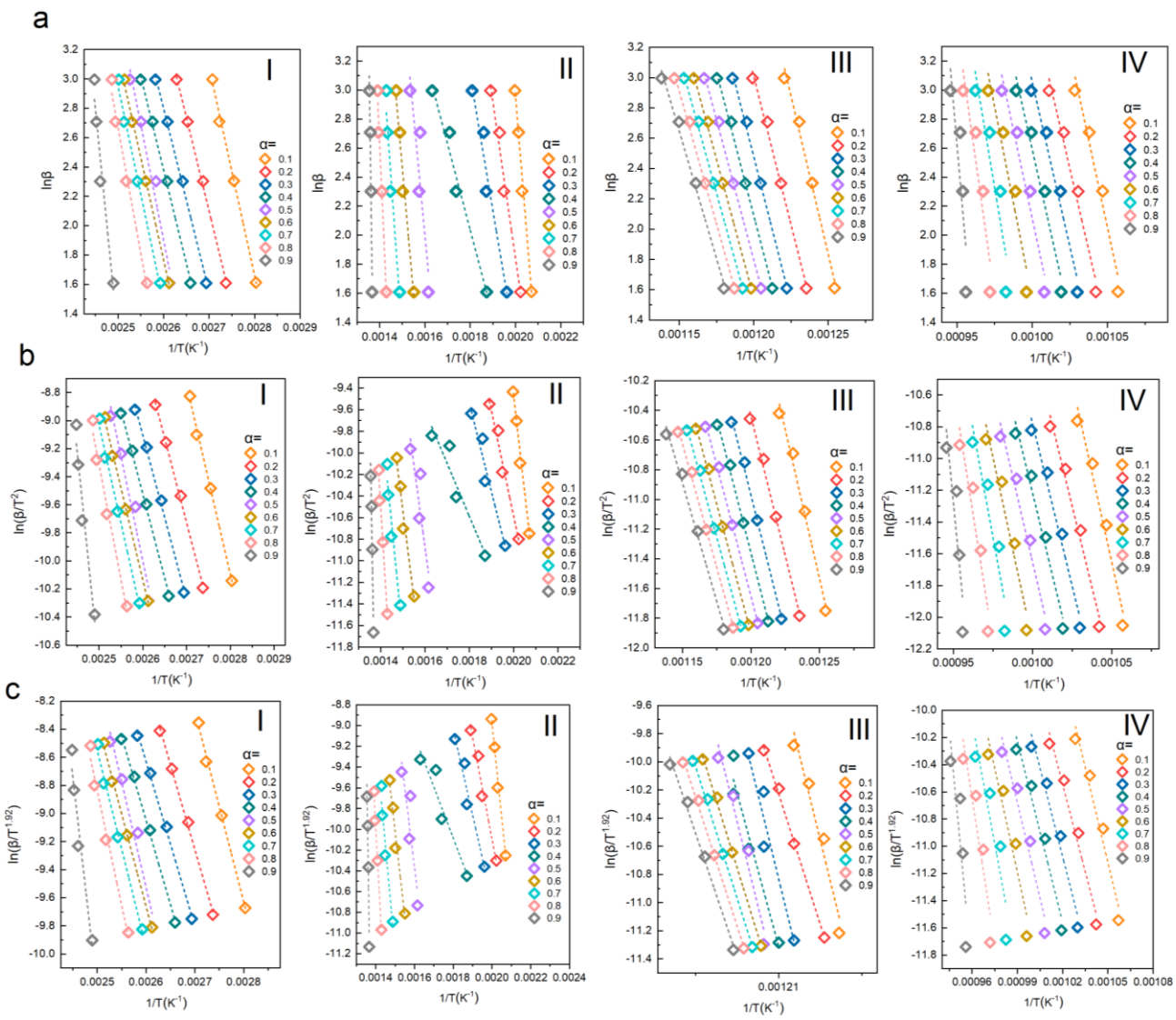

Figure S5. The linear fitting plots at different reaction stage through (a) FWO, (b) KAS, and (c) Starink methods.

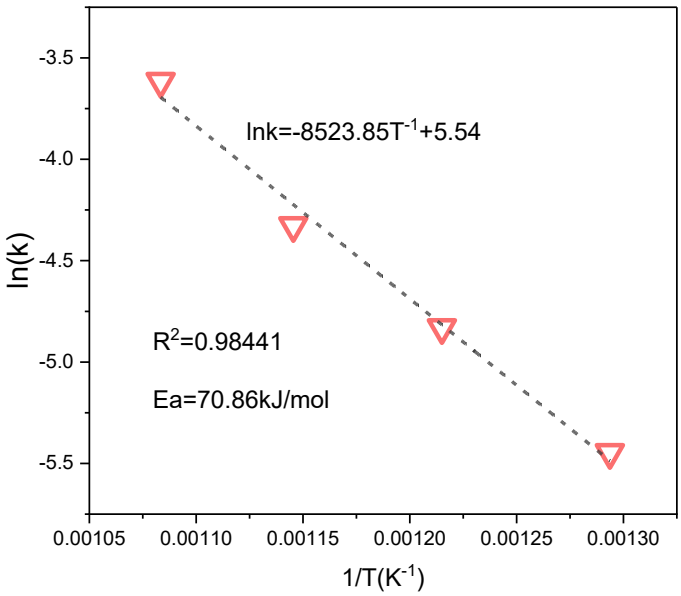

Figure S6. The linear fitting plot of ln(k(T)-1/T and calculated activation energy in first stage.

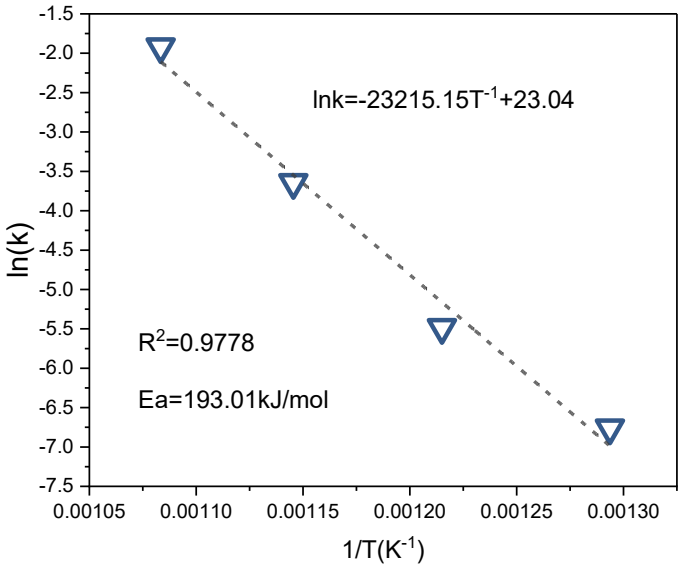

Figure S7. The linear fitting plot of ln(k(T))-1/T and calculated activation energy in second stage.

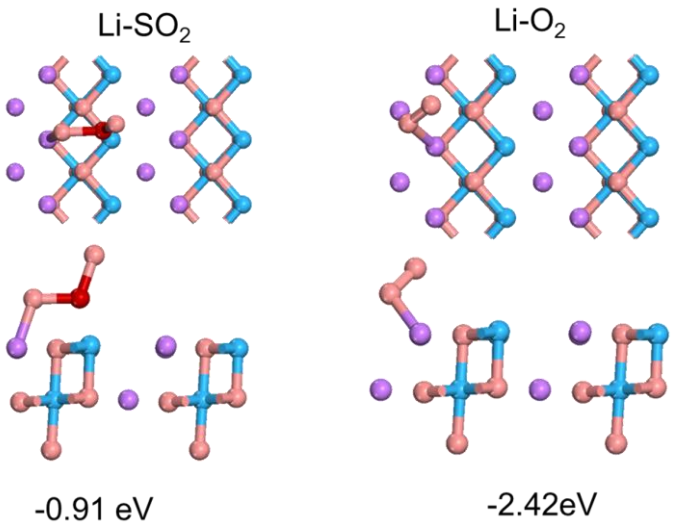

Figure S8. Adsorption energy of SO_2 and O_2 on Li over $LiCoO_2$ (104) surface.

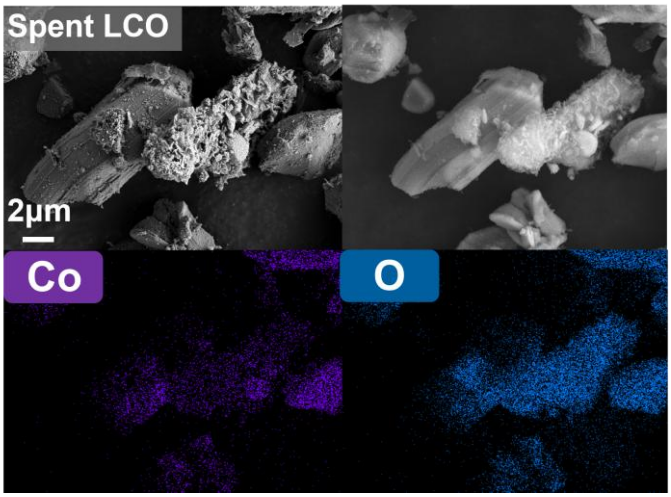

Figure S9. Scanning electron microscopy and energy-dispersive spectroscopy of spent $LiCoO_2$ active cathode material.

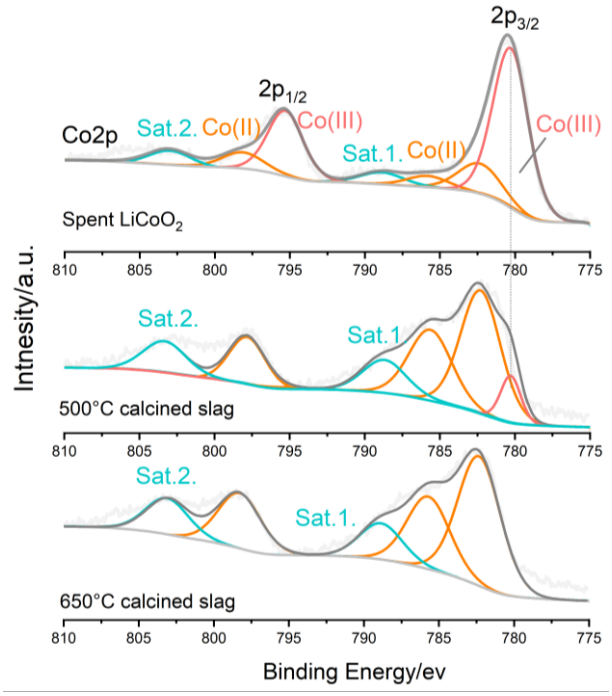

Figure S10. The spectra of Co2p obtained from the spent LCO cathode material and the roasted materials at different temperatures of 500°C and 650°C.

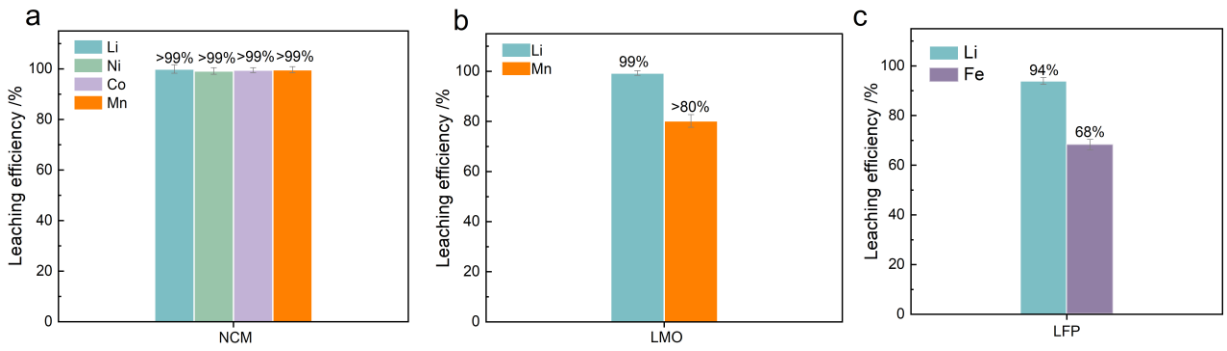

Figure S11. Leaching efficiencies of valuable elements from NCM (a), LMO (b), and LFP (c) under WFS-assisted sulfation roasting conditions.

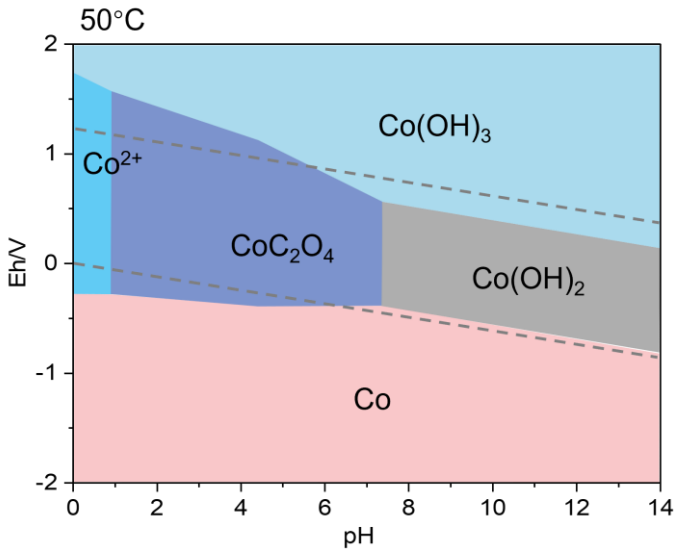

Figure S12. Eh-pH diagrams for Co-C_2O_4-H_2O system at 50°C.

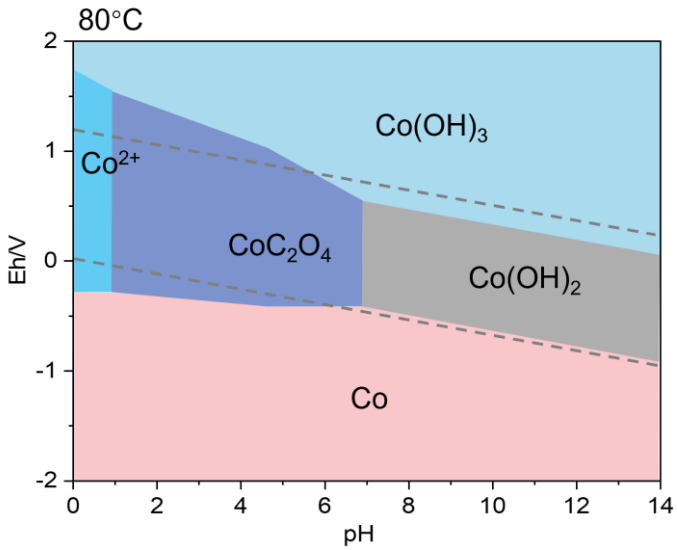

Figure S13. Eh-pH diagrams for Co-C_2O_4-H_2O system at 80°C.

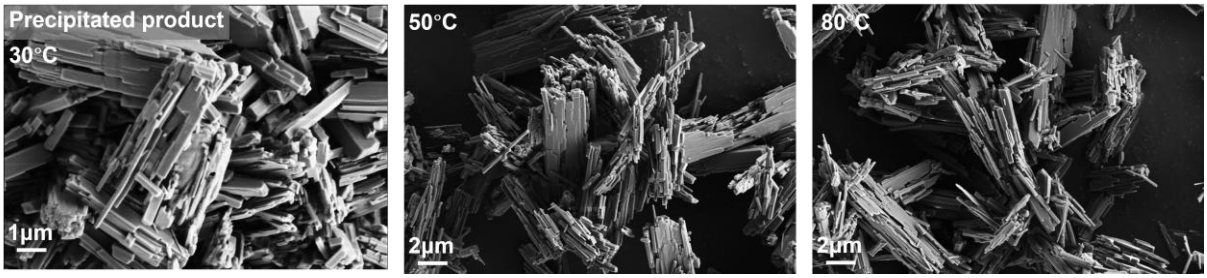

Figure S14. SEM analysis of obtained cobalt oxalate product.

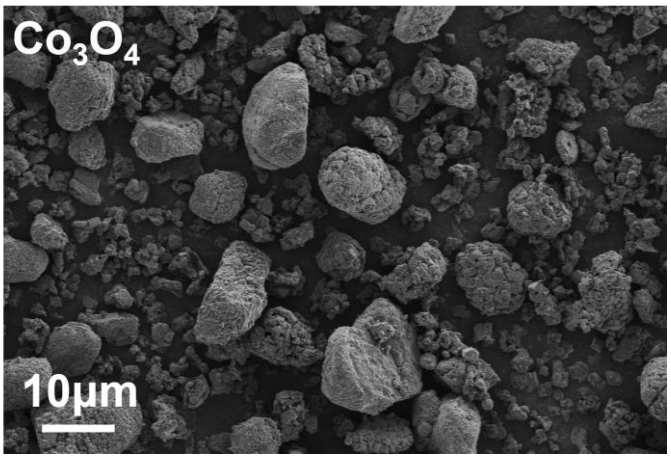

Figure S15. SEM analysis of obtained Co_3O_4 product.

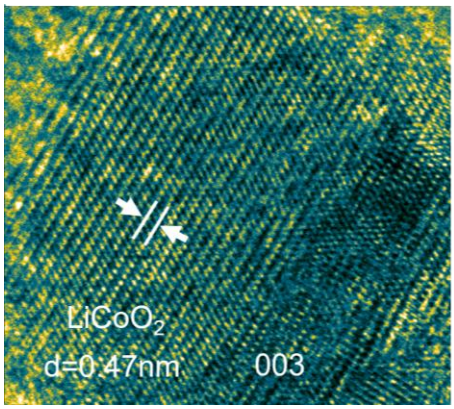

Figure S16. TEM analysis of obtained regenerated $LiCoO_2$.

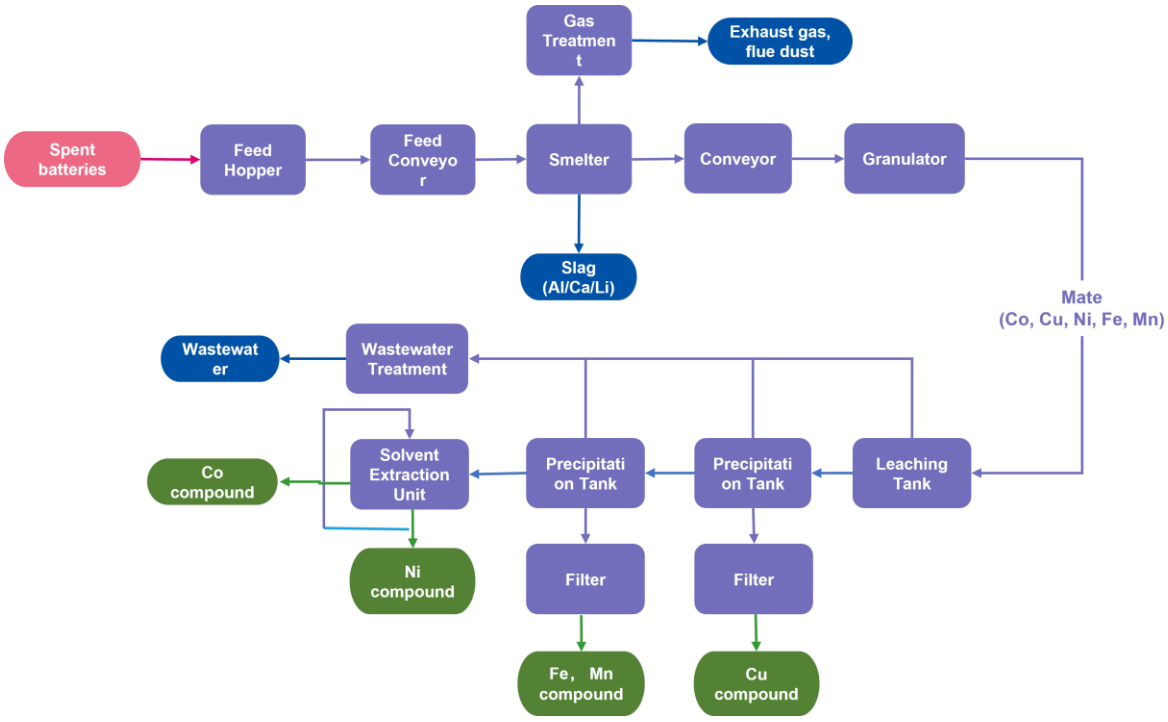

Figure S17. Process diagram of a generic pyrometallurgical recycling process.

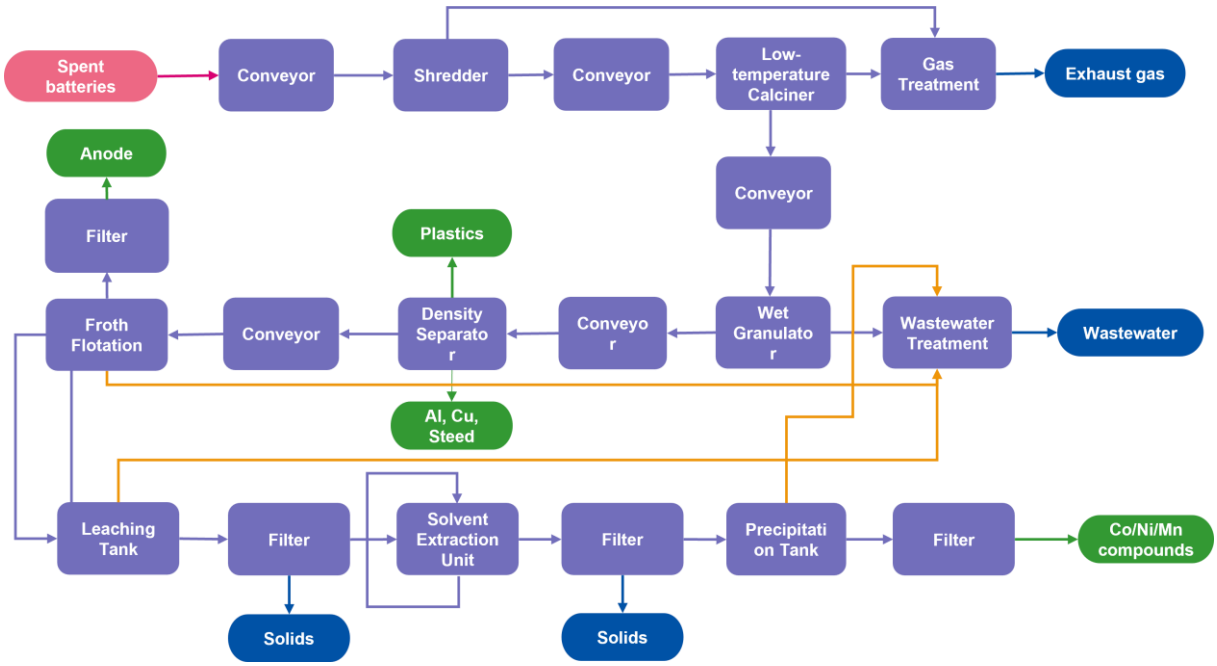

Figure S18. Process diagram of a generic hydrometallurgical recycling process.

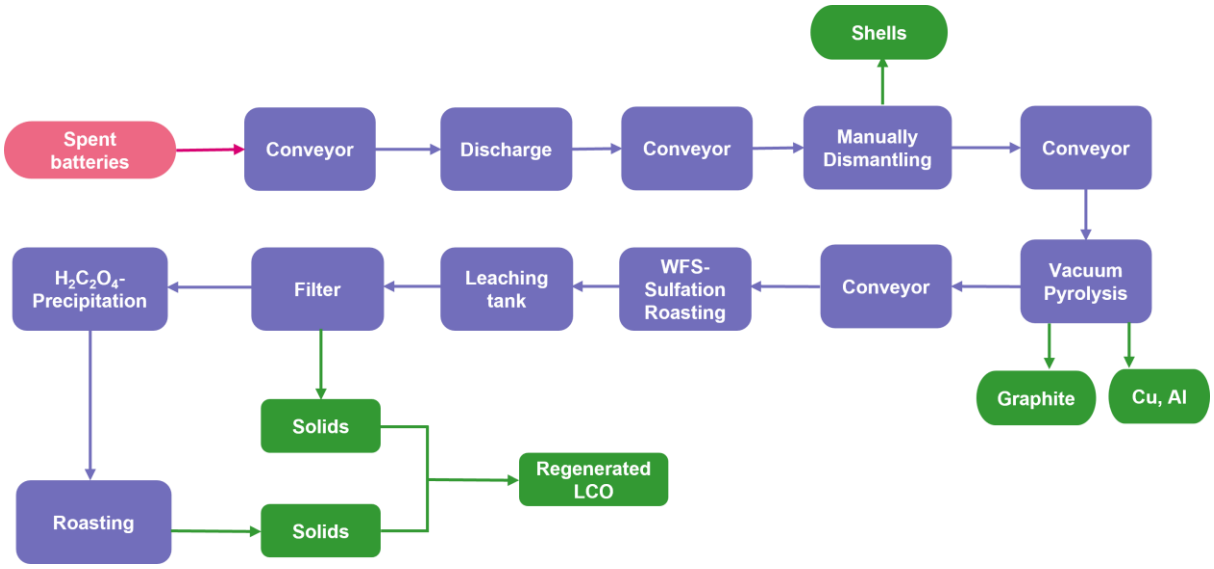

Figure S19. Process diagram of this recycling process.

Table S1. Chemical composition of the cathode powder of spent LCO battery (wt%).

Composition	Co	Li	Al	Ni	Mn	Fe	S	Ti	Mg
Cathode powder	54.44	6.72	0.10	0.06	0.01	-	-	-	-
WFS	-	-	0.03	-	-	34.09	18.93	0.84	1.2

Table S2. The G(α) of different reaction models.

Number	Abbreviation	Reaction Model	$G[(\alpha)]$
1	R1	One-dimensional phase boundary reaction	α
2	R2	Two-dimensional phase boundary reaction	$1-(1-\alpha)^{\frac{1}{2}}$
3	R3	Three-dimensional phase boundary reaction	$1-(1-\alpha)^{\frac{1}{3}}$
4	F1	First-order reaction	$-\ln(1-\alpha)$
5	F2	Second-order reaction	$(1-\alpha)^{-1}-1$
6	A3/2	Avrami-Erofeev, n=1.5	$[-\ln(1-\alpha)]^{\frac{2}{3}}$
7	A2	Avarmi-Erofeev, n=2	$[-\ln(1-\alpha)]^{\frac{1}{2}}$
8	A3	Avarmi-Erofeev, n=3	$[-\ln(1-\alpha)]^{\frac{1}{3}}$
9	A4	Avarmi-Erofeev, n=4	$[-\ln(1-\alpha)]^{\frac{1}{4}}$
10	D1	One-dimensional diffusion	α^2
11	D2	Two-dimensional diffusion	$\alpha+(1-\alpha)\ln(1-\alpha)$
12	D3	Three-dimensional diffusion (Jander equation)	$[1-(1-\alpha)^{\frac{1}{3}}]^2$
13	D4	Three-dimensional diffusion (Z-L-T equation)	$[(1-\alpha)^{-\frac{1}{3}}-1]^2$

Table S3. Materials and energy requirements to recycle 1 kg of spent batteries through different technologies (NR is not required).

	Pyrometallurgy	Conventional Hydrometallurgy	This work

Waste $FeSO_4 \cdot 7H_2O$	NR	NR	1.50
Ammonium hydroxide	NR	0.031	NR
Hydrochloric acid	0.21	0.012	NR
Hydrochloric peroxide	0.06	0.366	NR
Sodium hydroxide	NR	0.561	NR
Limestone	0.30	NR	NR
Sand	0.15	NR	NR
Sulfuric acid	NR	1.08	NR
Oxalic acid	NR	NR	0.45
Soda Ash	NR	0.02	0.02
Lithium Hydroxide	NR	NR	NR
Lithium carbonate	NR	NR	NR
Water consumption (gal)	NR	1	1

Table S4. Value of recycled materials ($/kg).

	Cathode product	Co^{2+} in product	Graphite	Aluminum	Copper
$/kg	45.53	52	0.2	1.45	5.43

Table S5. Material recovered from recycling process (kg/kg spent battery).

	Pyrometallurgy	Conventional Hydrometallurgy	This work
Copper	0.169	0.169	0.169
Aluminum	NR	0.085	0.085
Graphite	NR	0.175	0.175
Co^{2+} in product	0.238	0.238	NR
Cathode product	NR	NR	0.35

Table S6. The potential revenue of three recycling processes

	Pyro	Hydro	This work

Materials	Unit Prices ($/kg)	Recycled mass(kg)	Revenue ($)	Recycled mass(kg)	Revenue ($)	Recycled mass(kg)	Revenue ($)
		Revenue					
Copper	5.43	0.169	0.92	0.169	0.92	0.169	0.92
Aluminum	1.45	0	0	0.085	0.12	0.085	0.12
Graphite	0.2	0	0	0.175	0.04	0.175	0.04
Co^{2+} in output	52	0.238	12.38	0.238	12.38	0	0
Cathode product	45.53	0	0	0	0	0.35	15.94

Text S1:

Isothermal and non-isothermal kinetics:

For the sulfation roasting process, the primary focus is on investigating the reaction kinetics, particularly through non-isothermal kinetic analysis. Typically, the rate of a solid-state reaction can be expressed by Equation (S1), where k(T) is the temperature-dependent reaction rate constant, and $f(\alpha)$ is the differential model function describing the reaction mechanism. In non-isothermal kinetic analysis, o represents the extent of the reaction. Since non-isothermal experiments are conducted at a constant heating rate (β), the kinetic parameters are determined using mathematical fitting models. Specifically, the Kissinger-Akahira-Sunose (KAS) method (Equation S2), the Flynn-Wall-Ozawa (FWO) method (Equation S3), and the Starink method (Equation S4) are employed for this purpose.

$$\frac{d\alpha}{dt} = k(T)f(\alpha) \tag{S1}$$

$$\ln\left(\frac{\beta}{T^2}\right) = \ln\left(\frac{AR}{G(\alpha)E_a}\right) - \frac{E_a}{RT} \tag{S2}$$

$$ln\beta = \ln\left(\frac{AE_a}{G(\alpha)R}\right) - 5.331 - 1.051\frac{E_a}{RT} \tag{S3}$$

$$\ln\left(\frac{\beta}{T^{1.92}}\right) = constant - 1.0008\frac{E_a}{RT} \tag{S4}$$

Linear fitting of $\ln G(\alpha)$ versus $1/T$ was performed using Origin 2021. The accuracy of

the fitting was evaluated based on the adjusted R-squared (R^2) value and the consistency of the activation energy (Ea) calculated using the Kissinger-Akahira-Sunose (KAS), Flynn-Wall-Ozawa (FWO), and Starink methods. The $G(\alpha)$ functions for different reaction models are presented in the table, which are used to infer the reaction mechanism in non-isothermal kinetics. The integral Satava-Sestak method (Equation S5) was employed to fit the non-isothermal data, while the Coats-Redfern method (Equation S6) was also applied to support the exact mechanism at each step. The optimal mechanism function was estimated through linear fitting of $\ln G(\alpha)/T^2$ versus $1/T$.

$$\lg G(\alpha) = \lg\left(\frac{AE_a}{R\beta}\right) - 2.315 - 0.4567\frac{E_a}{RT} \quad \text{(S5)}$$

$$\ln\left(\frac{G(\alpha)}{T^2}\right) = \ln\left(\frac{AE_a}{R\beta}\right) - \frac{E_a}{RT} \quad \text{(S6)}$$

Text S2:

Regeneration of LCO

The Co_3O_4 obtained was wet-ground with Li_2CO_3 (Li/Co=1.05), and the resulted slurry was dried and further ground to ensure thorough mixing. The solid-state approach was employed to regenerate LCO by roasting the mixture at a heating rate of 2°C/min from air temperature to 800°C for 12 hours, resulting in the formation of regenerated $LiCoO_2$ (Re-LCO). The electrochemical characteristics of all cathode materials were evaluated using CR2032 button cells. A mixture of cathode material, polyvinylidene fluoride (PVDF), and acetylene black in an 8:1:1 mass ratio was mixed with N-methylpyrrolidone (NMP) to create a uniform slurry. This slurry was coated onto aluminum foil, dried in a vacuum oven at 120 °C for 10 hours. The electrolyte consisted of a 1 mol/L $LiPF_6$ solution in a solvent blend of ethylene

carbonate (EC), methyl carbonate (EMC), and dimethyl carbonate (DMC) in equal volume proportions, with a polypropylene separator utilized. Electrochemical charge/discharge and rate performance evaluations were conducted in the voltage range of 2.7 to 4.3 V (*vs* Li^+/Li) using NEWARE battery test system.

Text S3:

Economic and environmental analysis:

The EverBatt model can perform techno-economic and life-cycle analysis of three types of spent battery recycling processes: pyrometallurgy (Pyro), hydrometallurgy (Hydro), and this work in manuscript. It is a closed-loop battery recycling cost and environmental impacts model developed by Argonne National Laboratory. We select the Pyro and Hydro in the EverBatt model as a reference to assess this work (our cathode recycling (Waste $FeSO_4{\cdot}7H_2O$-assisted roasting and oxalic acid leaching recycling processes)) in respect of energy consumption, GHG (greenhouse gas) emissions, and economic benefits.

The recycling flow charts for the commercial pyrometallurgy, commercial hydrometallurgy in EverBatt model and our work are depicted in Figure S17, Fig. S18, and Fig. S19, respectively. The new direct recycling (This work) in the figure and the followings refer to the process of Waste $FeSO_4 \cdot 7H_2O$-assisted roasting and oxalic acid leaching recycling processes to recover $LiCoO_2$.

Figure S17 depicts the process of generic pyrometallurgical recycling. In the process, the spent batteries are sent to a smelter, and the electrolyte and plastics in the batteries are burned off to supply heat; graphite/carbon and aluminum in the batteries act as reducing agent for the

transition metals; Co, Cu, and Fe in the batteries end up in the matte; and the rest of the materials, including oxidized aluminum end up in the slag. The Co/Cu/Fe matte is then further leached by acid followed by solvent extraction and precipitation to produce cobalt and nickel compounds that can be used for new cathode materials production. It should be noted that lithium in the slag can potentially be recovered.

Figure S18 depicts the process of the generic hydrometallurgical recycling process. Firstly, the discharged and dissembled spent batteries are shredded and then undergo a low-temperature roasting process to burn off the binder and electrolyte, followed by several physical separation processes to separate out aluminum, copper, and steel as metal scraps and plastics. Then the anode is obtained after flotation and filtering, and a leaching process followed by solvent extraction and sometimes precipitation to produce Co compounds, and potentially lithium carbonate for new cathode material production.

Figure S19 depicts the direct recycling process of waste $FeSO_4 \cdot 7H_2O$-assisted roasting and oxalic acid leaching. In this process, the spent LIBs are discharged, disassembled, and undergo a series of physical separation processes to obtain plastics, metals, anode material, and cathode material. The waste $FeSO_4 \cdot 7H_2O$ and cathode powders are mixed and roasted, followed by filtration of the roasted product. Cobalt is precipitated using oxalic acid, while lithium is recovered via sodium carbonate precipitation, ultimately obtaining the LCO material precursor and achieving regeneration.

Evaluation of energy consumption and greenhouse gas emissions (GHGs)

Materials input

The materials requirements for the three recycling technologies are summarized in Table S3. The materials requirements for the pyrometallurgical and hydrometallurgical processes are obtained from EverBatt. The materials requirements for this work are obtained according to our experimental procedure. In the evaluation of the recycling process, the energy consumption and greenhouse gas emissions in the material production process are also considered.

Energy input

In order to calculate the impact of the various energy consumed in the process on the life cycle environment, the life cycle analysis will consider the environmental impact related to upstream fuel production and power generation, as well as the environmental impact related to on-site fuel combustion.

Process emissions

In the evaluation of greenhouse gas emissions EverBatt model also consider the environmental impacts related to process emissions. These GHG emissions are not caused by fuel combustion but are produced by the combustion of materials in the battery. GHG emissions are calculated based on 100-year global warming potentials from the fifth assessment report of the Intergovernmental Panel on Climate Change.

Evaluation of potential revenue

The revenue calculation was based on the sales of recycled materials. The prices and the quality of the various materials recovered are obtained from EverBatt and listed in Table S4-S6. Revenues are calculated as:

$$\text{Revenue} = \sum m_i \times up_i$$

Where m_i (g/L) is the mass of material i recovered from spent batteries; and up_i is the unit price of material i as shown in Table S4.

Text S4:

Analysis method:

The solid samples underwent examination using a Bruker D8 Advance X-ray diffractometer with Cu Kα radiation (λ=1.5406Å). The diffraction patterns were obtained by scanning the 2θ range from 10° to 80°. Additionally, to assess metal concentrations in the leachate, an ICP-OES analyzer (ICAP 7000, Thermofisher) was used. The morphology and elements contents in the surface of solid samples were evaluated using a 20 kV SEM, namely the Hitachi S4800 model from Japan. To investigate the thermal characteristics of the LCO and the mixture with WFS, thermal gravimetric analysis (TGA) was performed using a Pris 1 TGA instrument under an air flow environment. HSC Chemistry 9.0 program was used to determine thermodynamic parameters such as free energy changes, standard Gibbs enthalpy changes, and equilibrium composition of processes involving $LiCoO_2$, $FeSO_4 \cdot 7H_2O$. The morphologies and crystal structures of spent LCO and roasting slag were analyzed by high resolution transmission electron microscopy (HRTEM, JEOL, JEM-2100 plus). The chemical condition of the electrode materials and solid pyrolysis products was investigated using X-ray photoelectron spectroscopy (XPS, AXIS Ultra DLD, Kratos, Japan).

Geometric optimization was conducted using the CASTEP module within Materials Studio, employing Density Functional Theory (DFT). The Perdew-Burke-Ernzerhof (PBE)

functional, a Generalized Gradient Approximation (GGA) employing, was employed. For rigorous convergence, parameters such as the plane wave energy cutoff, energy convergence, and force convergence were set to 400 eV, 1×10^{-5} eV, and 0.03 eV/Å, respectively. The adsorption energy (Ea) can be determined using Equation :

$$E_a=E_{LiCoO_2+gas}-E_{LiCoO_2}-E_{gas}$$

In equation , $E_{LiCoO2+gas}$ represents the total energy of the gas adsorption system on $LiCoO_2$ surface, E_{LiCoO2} is the total energy of the $LiCoO_2$ surface, and Egas is the total energy of the gas molecule.

Text S5:

Equilibrium calculations:

In the cobalt ion oxalate precipitation system, cobalt ions can precipitate with oxalate ions, hydrogen oxalate ions, and other species. The equilibrium constants for the main reactions are as follows:

$$Co^{2+} + C_2O_4^{2-} = Co(C_2O_4^{2-})^0(s) \qquad LogK_{sp}=7.26$$

$$Co^{2+} + 2C_2O_4^{2-} = Co(C_2O_4^{2-})_2^{2-} \qquad LogK_{sp}=6.70$$

$$Co^{2+} + 3C_2O_4^{2-} = Co(C_2O_4^{2-})_3^{4-} \qquad LogK_{sp}=9.70$$

$$Co^{2+} + C_2O_4^{2-} = Co(C_2O_4^{2-})^0 \qquad LogK_{sp}=4.79$$

$$Co^{2+} + HC_2O_4^{-} = Co(HC_2O_4^{-})^+ \qquad LogK_{sp}=1.61$$

$$Co^{2+} + 2HC_2O_4^{2-} = Co(HC_2O_4^{-})_2^{-} \qquad LogK_{sp}=2.89$$

$$Co^{2+} + OH^{-} = Co(OH)^+ \qquad LogK_{sp}=4.30$$

$$Co^{2+} + 2OH^{-} = Co(OH)_2(s) \qquad LogK_{sp}=14.9$$

$$Co^{2+} + 3OH^- = Co(OH)_3^- \qquad LogK_{sp}=9.70$$

$$Co^{2+} + 4OH^- = Co(OH)_4^{2-} \qquad LogK_{sp}=10.2$$

$$Co^{2+} + 2OH^- = Co(OH)_2 \qquad LogK_{sp}=8.4$$

Meanwhile, there are also equilibrium reactions of oxalic acid in the precipitation solution system, as follows:

$$H_2C_2O_4 = HC_2O_4^- + H^+ \qquad LogK_{sp}=-1.271$$

$$H_2C_2O_4 = C_2O_4^{2-} + H^+ \qquad LogK_{sp}=-4.272$$

Based on the principle of mass balance in the precipitation system and incorporating the above equilibrium data, the following equilibrium expressions can be derived:

$[Co]_T=[Co^{2+}]+[Co(C_2O_4^{2-})_0]+[Co(C_2O_4^{2-})_2^{2-}]+[Co(C_2O_4^{2-})_3^{4-}]+[Co(OH)_2]+[Co(HC_2O_4^{2-})^+]+[Co(HC_2O_4^{2-})_2]+[Co(OH)^+]+[Co(OH)_3^-]+[Co(OH)_4^{2-}]$

$[C_2O_4^{2-}]_T=[C_2O_4^{2-}]+[HC_2O_4^{2-}]+[H_2C_2O_4]+[Co(C_2O_4^{2-})_0]+2\times[Co(C_2O_4^{2-})_2^{2-}]+3\times[Co(C_2O_4^{2-})_3^{4-}]+[Co(HC_2O_4^{2-})+]+2[Co(HC_2O_4^{2-})_2]$

$[OH]_T=[OH^-]+[Co(OH)^+]+2\times[Co(OH)_2]+3\times[Co(OH)_3^-]+4\times[Co(OH)_4^{2-}]$

Meanwhile, based on the ionization equilibrium of oxalic acid and its constants, the following expression can be derived:

$$[C_2O_4^{2-}] \cdot [H^+]/[HC_2O_4^-] = K = -4.272$$

$$[HC_2O_4^-] = [C_2O_4^{2-}] \cdot [H^+]/K = 10^{-pH} \cdot 10^{-4.27} \cdot [C_2O_4^{2-}] = 10^{4.27-pH} \cdot [C_2O_4^{2-}]$$

Similarly, based on the reaction $Co^{2+} + C_2O_4^{2-} = Co(C_2O_4^{2-})^0$, the following expression can be derived:

$$[Co(C_2O_4^{2-})^0]/[Co^{2+}][C_2O_4^{2-}] = K = 4.79$$

$$[Co(C_2O_4^{2-})^0] = [Co^{2+}][C_2O_4^{2-}] \cdot K = 104.79[Co^{2+}] \cdot [C_2O_4^{2-}] \cdot 10^{4.27}$$

$$[Co(C_2O_4^{2-})_3^{4-}] = [Co^{2+}] \cdot [C_2O_4^{2-}]^3 \cdot 10^{9.7}$$

$$[Co(HC_2O_4^-)_2] = [Co^{2+}] \cdot [C_2O_4^{2-}]^2 \cdot 10^{11.43-2*pH}$$

$$[Co(C_2O_4^{2-})_2^{2-}] = [Co^{2+}] \cdot [C_2O_4^{2-}]^2 \cdot 10^{6.7}$$

$$[Co(C_2O_4^-)^+] = [Co^{2+}] \cdot [C_2O_4^{2-}]3 \cdot 10^{5.88-pH}$$

In addition, the precipitation of cobalt oxalate also involves a precipitation equilibrium. Based on the solubility product (Ksp), the following equilibrium expression can be established:

$$[Co^{2+}] = K_{sp}/[C_2O_4^{2-}]$$

As the pH increases to alkaline conditions, the oxalate precipitate transforms into a hydroxide precipitate. The equilibrium expression at this point is:

$$[Co^{2+}] = K_{sp}/[OH^-]^2 = K_{sp} \times 10^{28-2*pH}$$

$$[Co^{2+}] = \min\{K_{sp}/[C_2O_4^{2-}], K_{sp} \times 10^{28-2*pH}\}$$

With an oxalate ion concentration of 0.6 mol/L, and based on the proportions of each component, the distribution diagram of the components can be obtained.